

Skew scattering and ratchet effect in photonic graphene

O.M. Bahrova^{1,2} and S.V. Koniakhin^{1,3}

¹*Center for Theoretical Physics of Complex Systems,
Institute for Basic Science (IBS), Daejeon 34126, Republic of Korea*

²*B. Verkin Institute for Low Temperature Physics and Engineering of the National
Academy of Sciences of Ukraine, 47 Nauky Ave., Kharkiv 61103, Ukraine*

³*Basic Science Program, Korea University of Science and Technology (UST), Daejeon 34113, Republic of Korea*

In this paper we bring up our investigation on the properties of asymmetric scattering in graphene made with the microcavity exciton-polaritons. It is shown by numerical simulations of Gross-Pitaevskii equation that ratchet phenomena occurs in the polariton graphene due to its structural inhomogeneity. Thus, we suggest a way to induce preferential motion of polaritons by the confinement potential engineering.

I. INTRODUCTION

In the domain of condensed matter physics, the study of exciton-polaritons has emerged as a captivating direction, offering a unique blend of quantum optics and solid-state physics. Exciton-polaritons, including them existing in semiconductor microcavities, are hybrid quasiparticles arising from the strong coupling [1] of 2D confined excitons and long-living photons in specially engineered optical cavities [2]. Due to composite nature sharing properties of light and matter [3], multiple non-trivial phenomena were observed in the systems of exciton-polaritons [4, 5]. Often, these phenomena have analogues in other condensed matter systems. For example, polaritons manifest possibility to condensate at high temperatures [6]. The effects of superfluidity [7] and soliton emergence allow attributing the polariton systems as “quantum fluids of light” [8–10]. Abrikosov vortices have their counterparts in polariton systems [11, 12], and the complex phenomenon of quantum turbulence [13–15] is also of high interest in that context. Exciton-polaritons offer flexible all-optical control of excitation [16] and various detection techniques for cw and time-resolved measurements of photon emission spatial profile, momentum-domain emission and energy dispersion. As a result, all mentioned above phenomena can be experimentally investigated with unprecedented level of details and entirety. The artificial optical lattices obtained by advanced microcavity etching techniques are of particular interest.

Photonic lattices have gained significant attention due to the ability to both mimic certain phenomena observed in real 2D crystals and practically implement theoretical concepts lacking analogues in nature. A site in such structures is a single micropillar [17] and further these micropillars can be organised into complicated arrays [18–20]. Similar to electronic band structures in graphene [21], photonic honeycomb lattices exhibit the formation of Dirac cones in the band structure and the associated linear dispersion relation [22, 23]. Thus, here are extensive studies of the topological and transport properties of artificially created graphene-type lattices [19, 24–26]. Generally, topological photonics is among hot topics of modern physics nowadays. It opens a path towards the

investigation of fundamentally new states of light and potential applications of topological phenomena in the development of robust and scalable quantum devices [27–29]. Manifestation of topologically protected edge states and the associated quantum Hall-like effects [19, 22, 30] in microcavity polariton lattices allows them to gain significant attention. The closely related phenomenon is Hall effect (both in optical and electronic systems including the variations like spin Hall effect, valley Hall effect etc.). Its origin can lie in manifestation of geometric phase or in the effect of asymmetric scattering.

Asymmetric (i.e., skew) scattering in physics refers to a type of scattering process where the probabilities of scattering into different directions are not symmetrical with respect to the incident direction [31]. It introduces directionality which can arise from structural asymmetries, non-uniform potentials, or the presence of external fields, etc., into scattering processes, where certain directions become favored or disfavored based on the system’s characteristics. This phenomenon can occur in various physical systems [27, 32, 33] and understanding asymmetric scattering is crucial for interpreting experimental results and designing devices with specific functionalities.

Furthermore, a spatial inversion symmetry breaking, including that originated from the defects of particular symmetry, in electronic or mechanical systems can lead to the so-called ratchet effect. The ratchet effect itself can be referred as appearance of steady unidirectional response to oscillating or stochastic driving excitation [31]. The geometry of ratchet effect is defined by global symmetry of the system and for the relevant case of C_{3v} symmetry, one can expect appearance of vertical response component for driving force applied horizontally [34].

In graphene under asymmetric periodic strain the classical ratchet effect was considered [35], see also Ref. [36, 37]. Moreover, the magnetic ratchet electron motion in a two-dimensional electron gas [38] and single graphene layer [32, 39] which is subject to the static magnetic and alternating electric fields, was observed. Asymmetry in the geometry of microstructure can be a basis to implement the diode device [40], which is closely related to the field of ratchet studies.

As mentioned above, asymmetric (skew) scattering is

one of the possible underlying mechanisms for realization of ratchet effect. Thus, the skew scattering on semidisk Galton board [41, 42] and triangular defects [34] was proven to originate ratchet effect in low-dimensional structures and graphene, see also Ref. [43].

In the present paper we demonstrate a possibility to observe ratchet effect in photonic graphene as a consequence of skew scattering on triangular C_{3v} symmetry defects embedded into regular honeycomb lattice. The remainder of this paper is organized as follows. In the beginning of Sec. II the model system based on a polariton analog of graphene with triangle-shaped defects is introduced. Then, by means of effective Schrödinger equation for exciton-polaritons, we study in details properties of the asymmetry in scattering. We derive scattering cross-sections and indicatrices for the wave packet with a specific wave vector being scattered on a single triangular defect in classical and quantum regimes. Further, in Sec. III, we explore setup of the honeycomb lattice with multiple randomly distributed defects and provide results of corresponding numerical simulations. We propose a simple scheme to observe the emergence of ratchet effect based on the platform of exciton-polaritons with real-space time-integrated intensity measurements. In Sec. IV we establish connection between the results from previous sections with that obtained employing Monte-Carlo simulations being a simple realization of kinetic approach. Finally, in Sec. V, we conclude the paper with a summary and an outlook.

II. SKEW SCATTERING BY SINGLE TRIANGLE

In this work, we consider optical exciton-polariton analog of a single-layer graphene. That system has experimental realization via microcavity etching resulting in the overlapped micropillars arranged into honeycomb lattice [44, 45]. We focus on the ratchet effect originated from skew scattering by the defects of particular shape. Specifically, the equilateral triangle-shaped defects (C_{3v} symmetry) are embedded into graphene lattice as missing micropillars (sites), see Fig. 1. Formally, presence of such defects breaks the spatial inversion symmetry of a system and provides the global C_{3v} symmetry.

We investigate time evolution of a wave packet (or initial wave function engineered in differing way) in linear regime and perform numerical simulations of the effective Schrödinger equation widely used to trace dynamics of exciton-polaritons at low densities:

$$i\hbar \frac{\partial \psi}{\partial t} = \left[-\frac{\hbar^2}{2m} (\partial_x + \partial_y) + V - i\hbar \frac{\gamma}{2} \right] \psi. \quad (1)$$

Here $m = 5 \cdot 10^{-5} m_e$ is the effective polariton mass, $\gamma \equiv \gamma_0 f(x, y)$ stands for polariton decay rate, $V(x, y)$ describes the confinement potential (3 meV for the barrier height) defined by the shape of honeycomb lattice of micropillars with embedded triangular defects as it

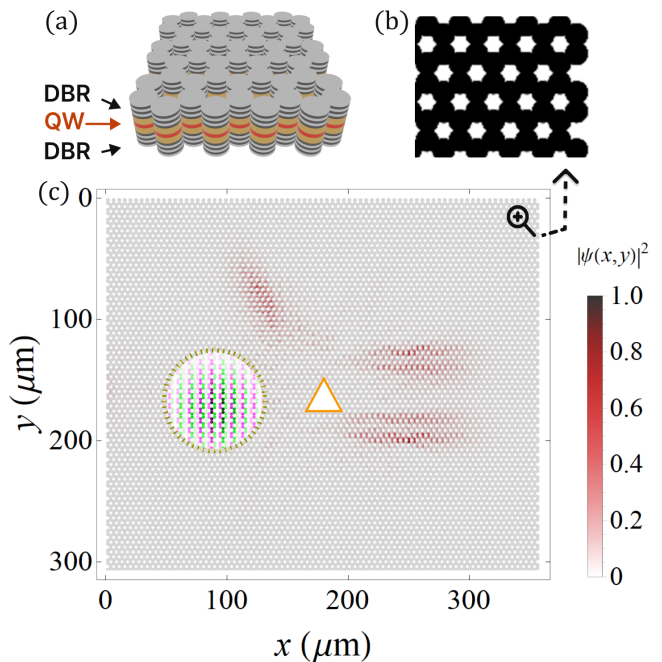


Figure 1. Demonstration of asymmetric Gaussian wave packet scattering on triangular defect (orange triangle) embedded into polariton graphene lattice (shown in gray in the main figure). The yellow circle indicates the half-width of the initial Gaussian-shape wave function. Green-purple colors with intensity modulation show phase profile of the wave packet for wave vector $q = 0.2$, the color intensity is proportional to the wave function amplitude squared.

is shown in Fig. 1. We perform integration of Eq. (1) on the 2048×2048 square mesh grid with $0.2 \mu\text{m}$ spatial step using the third-order Adams-Bashforth method with time step $\delta t = 2 \times 10^{-5}$ ps and putting into service Graphics Processing Unit (GPU) for acceleration. The pillar size corresponds to the one in experimental samples from Refs. [45]. At the same time, the obtained results are valid for the optical realization of graphene by means of electromagnetic induced transparency (EIT) effect in atomic vapor cells [24, 46, 47].

As a first step, we investigate properties of scattering on a single triangle-shaped defect. Thus, for the initial condition a plane wave modulated by a Gaussian function is as follows:

$$\psi_{in} = \frac{1}{N} \exp \left[-\frac{(x - x_0)^2}{2R_0^2} - \frac{(y - y_0)^2}{2R_0^2} + \mathbf{k}\mathbf{r} \right], \quad (2)$$

with the wave vector component values $\mathbf{k} = (k_x, k_y)$ taken in the proximity of Dirac points within the first Brillouin zone: $\mathbf{k} = \mathbf{k}_D - \mathbf{q}$, where \mathbf{k}_D stands for Dirac point wave vector. N is a normalization constant; R_0 describe the size of the wave packet as it is shown in Fig. 1 by the yellow dashed circle.

One can characterize a scattering process via determination of the differential cross-section specifying the

angular distribution of the scattered wave function. In Figure 2 one can see the calculated scattering diagrams $W_{0^\circ, \varphi'}$ that yield the fraction of optical signal ($|\psi|^2$) scattered in a given direction φ' for the 0° incident direction as it is presented in Fig. 1. We take wave packet size $R_0 = 90$ nm to be much greater than the wave packet wave length. We take into account defects of different sizes covering various regimes of wave vector scattering: from quantum to classical. The initial wave vector has its component only in the x direction with the value $q \equiv |\mathbf{q}| = 0.2$ measured from the Dirac point $\mathbf{k}_D = (2\pi/(3\sqrt{3}a), 2\pi/(3a))$ with a being the lattice constant.

The following hierarchy of the size scales takes place in setup under consideration. In quantum mechanical (wave) regime $R_0 \gg L \gtrsim \lambda$, the wave packet size is greater than defect size L and the latter is greater than wave length $\lambda = \frac{2\pi}{q}$. By increasing size of the defect, one can approach the regime $L \gtrsim R_0 \gg \lambda$ corresponding to classical mirror reflection. In both cases, wave length is the lowest size scale. In the case of small defects $L < \lambda$ (Rayleigh limit), scattering efficiency, including the asymmetric part, becomes too low to have manifestation in detectable ratchet flux.

To focus on the scattering process itself, we take $\gamma_0 = 0$ thus assuming the polariton lifetime being much longer than the time required for the scattering process to occur. This assumption should be also valid for EIT-based realizations of photonic graphene in atomic vapor cells [24]. Then, in order to characterize the asymmetry of scattering, we introduce the asymmetry parameter [48] $\mathbf{g} \equiv (g_x, g_y)$ defined as average cosine (sine) of scattering angle: $(g_x, g_y) = (\langle \cos \varphi \rangle, \langle \sin \varphi \rangle)$,

$$g_{\{x,y\}} = \frac{1}{w} \int_0^{2\pi} \{\cos \varphi, \sin \varphi\} W_{0^\circ, \varphi} d\varphi, \quad (3)$$

which quantify asymmetry along horizontal (g_x) and vertical (g_y) axes; $w = \int_0^{2\pi} W_{0^\circ, \varphi} d\varphi$. Thus, using this approach, we become capable to classify polar scattering diagrams as shown in Fig. 2(c), where the component dependencies of the asymmetry vector on the defect size are plotted (red and green markers, respectively). For comparison, we also present data for the similarly defined transport (momentum transfer) cross-section $\sigma_{tr} = \langle 1 - \cos \varphi \rangle$ (black dots). The dashed lines indicate linear fitting drawn as the guide for an eye. The linear dependence of asymmetry in scattering versus triangle size has been predicted for regular graphene [34]. Note that $g_{x(y)}$ takes values in the range $[-1, 1]$ by definition, $\mathbf{g} = (1, 0)$ corresponds to the limit of absence of a scatterer. Apparently, Fig. 2(c) shows that g_y is always positive which reflects the fact of prevailing of scattering in the upper semiplane, see Fig. 2(a). Moreover, $g_x > 0$ is related to the case when a defect scatters more wave function toward the forward direction ($\varphi' = 0$), and vice versa, $g_x < 0$ when the back-scattering ($\varphi' = \pi$) prevails. According to g_x and g_y behaviors, the transition from

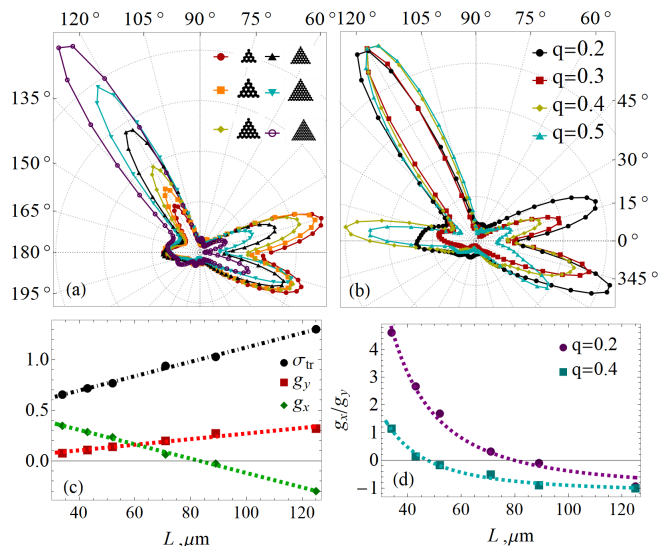


Figure 2. Scattering indicatrices for triangular defect of various sizes (a) and values of the initial wave vector (b). The black curve is common in panels (a) and (b). Panel (c) shows the coefficients of scattering asymmetry $g_{x,y}$ along horizontal x and vertical y axes (red and green markers, respectively), given by Eq. (3), for $q = 0.2$ and compared with the transport cross-section σ_{tr} (black dots). The dashed lines mark the linear fit. Panel (d) represents the ratio of g_x/g_y versus size of the triangle defect L . Dashed curves correspond to $1/x^2$ fit.

quantum to classical mirror reflection regime takes place at approximately 90nm, which matches with high precision with the wave packet size. Finally, Fig. 2(d) shows the ratio of g_x/g_y versus size of triangle L for two values of initial wave vector $q = 0.2$ (purple dots, associated with (a) and (c) subfigures) and $q = 0.4$ (rectangles, see also *Supplemental Materials*). As it is evident from Fig. 2(c), $\alpha/L^2 - 1$ fitting is appropriate to utilize (α is a fitting parameter).

As a next step, it becomes essential to construct full scattering rate matrices in respect to all regimes of scattering as it follows from the above consideration. Thus, scattering diagrams for six incident and scattering directions (the only allowed in classical mirror reflection limit) have been calculated. The scattering rate $W_{k,k'}$ defines probability distribution for an incident direction k to one of scattering k' . Figures 3-4 show scattering rate matrices with its symmetric and anti-symmetric parts in two opposite regimes of scattering: classical and quantum, respectively, see also *Supplemental Materials*. One could make a correspondence between Fig. 3(a) and the purple curve as well as Fig. 4(a) with the red curve in Fig. 2(a).

III. RATCHET EFFECT

In the present section we demonstrate how skew scattering on triangular defects leads to ratchet effect in the whole system and quantitatively characterize it. Here,

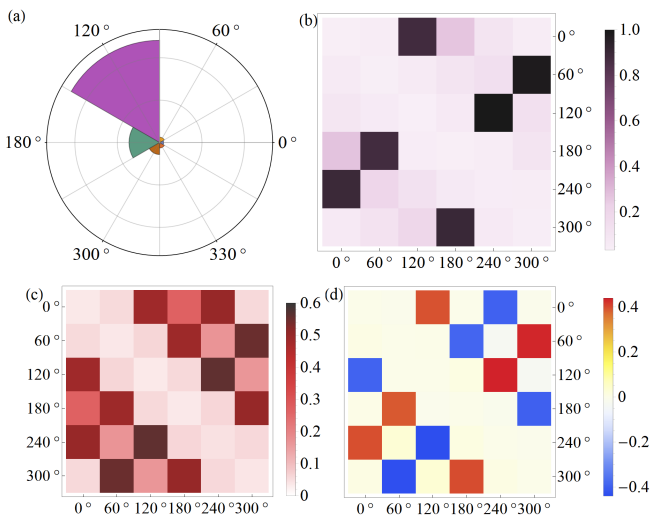


Figure 3. Panel (a). Scattering diagram for scattering process with geometry as in Fig. 2 in classical regime $L > R_0$ (defect is larger than wave packet size). Panel (b). Scattering rate $W_{k,k'}$ matrix for six discrete directions of wave vector. Panels (c) and (d) show decomposition of scattering matrix into symmetric ($W_{k,k'}^{(s)}$) and anti-symmetric ($W_{k,k'}^{(a)}$) parts, respectively. Noteworthy, panel (a) in fact represents the values $W_{0,k'}$.

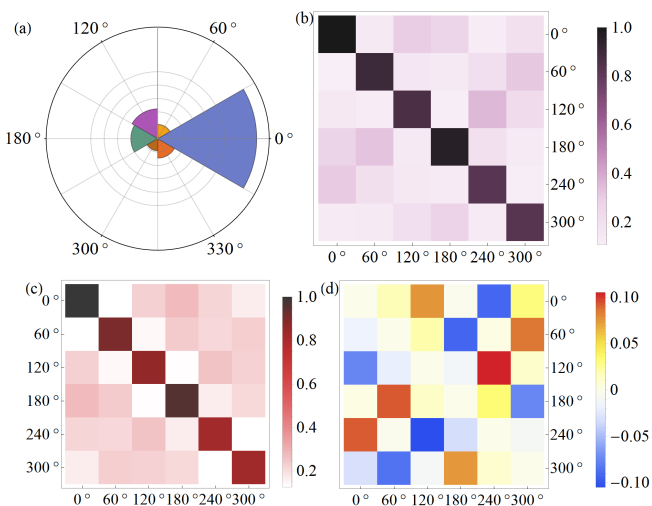


Figure 4. Scattering diagram and scattering rate matrices for wave regime $R_0 \gg L$.

we consider an array of randomly distributed defects between upped and lower absorbers characterized by finite polariton losses $\gamma(x, y)$. Importantly, despite random positions, the defects are coherently oriented, which provides the global C_{3v} symmetry for the system required to observe the ratchet effect. The absorbers exclude effects of scattering from the boundaries. The employed decay rate spatial profile is homogeneous in horizontal direction and its vertical profile $\gamma(x, y) \equiv \gamma(y)$ is shown in Fig. 5(a) with the white dashed curve. Maximal mag-

nitude of the decay rate equals $\gamma_0 = 10 \text{ ps}^{-1}$. We start from a white noise-like wave function of random phase and amplitude at each site (see *Supplemental Materials*) to demonstrate resulting unidirectional response.

In order to quantitatively characterize manifestation of the ratchet effect, we integrate over time the wave function ($|\psi|^2$) in the upper and lower counting regions denoted by pink and red lines in Fig. 5(a) and placed slightly prior to the absorbers. The counting regions are symmetric with respect to a perfect structure horizontal symmetry axis and to the absorbers. To exclude the effect of statistical asymmetry, the triangular defects are placed in equivalent fractions above and below the symmetry axis. Figure 5(a) shows the intensity profile of wave function after 90 ps of time evolution.

In Figure 5(b) we plot the instantaneous characteristic of asymmetry in resulting ratchet flux, i.e. difference the in intensities for the upper and the lower counting regions at a given time moment t :

$$\Delta(t) = \frac{I_{\text{up}}(t) - I_{\text{d}}(t)}{0.5 \cdot (I_{\text{up}}(t) + I_{\text{d}}(t))}, \quad (4)$$

where $I_{\text{up(d)}}(t) = \int_{\text{up(d)}} |\psi(x, y, t)|^2 dx dy$, for different realizations (colors) of initial conditions for the wave function. The black dots correspond to the averaged values. Further, Fig 5(c) shows integral characteristic being the ratio of time-averaged intensities between the upper (up) and the lower (d) counting regions

$$I_{\text{up(d)}}^{(\text{tot})}(t) = \frac{1}{t} \int_0^t I_{\text{up(d)}}(t') dt'.$$

IV. KINETIC APPROACH TO RATCHET EFFECT

In present section, we aim to establish connection between the derived scattering cross sections (Sec. II) for single triangle and observed macroscopic ratchet effect in the system (Sec. III) by means of statistical approach and Monte-Carlo simulations.

To do so, we implement the simulation of carrier random walks with six discrete directions of motion corresponding to the angles in panels (a) of Figs. 3-4. At each time step the particle might move at distance dl or undergo scattering process with a small probability $p_{dl} = n\sigma dl$. The integral cross section can be estimated as triangle size: $\sigma \approx L$. Scattering probabilities for various incident and resulting angles are encoded in (b) panels of Figs. 3-4. Finally, scattering rate is proportional to the concentration of defects (triangles) n taken as in the setup used for the Schrödinger equation simulations discussed above. The initial position of the particle (x_0, y_0) is chosen to be arbitrary within the sample size L_0 and motion direction is taken randomly from 6 allowed values, which mimics the noise-like wave function used in Schrödinger equation simulations.

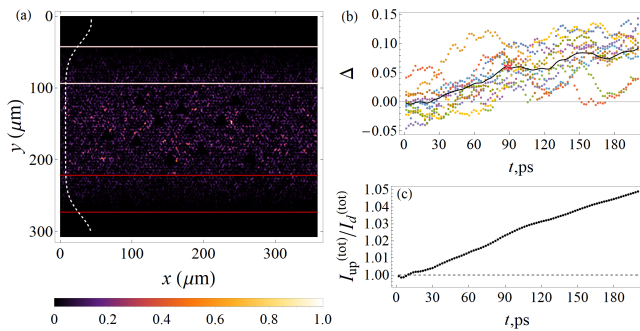


Figure 5. Illustration of macroscopic ratchet effect in the system. (a) The wave function $|\psi(x, y)|^2$ for $t = 90ps$ (marked by the red star in (b)). The light-red and dark-red lines show the wave function counting regions for comparison of upwards and downwards fluxes, respectively. The white dashed curve indicates the spatial decay rate profile $\gamma(y)$. (b) The difference Δ of total emission intensity (proportional to polariton density $|\psi|^2$) from upper (up) and lower (d) counting regions over time for various initial wave functions (in colors) and the average value (black curve). (c) The ratio of time-averaged wave function in upper region $I_{\text{up}}^{(\text{tot})}$ to the one in lower counting region $I_{\text{d}}^{(\text{tot})}$ versus time (averaged over 10 realizations as showed in (b)).

We have run a set of multitudinous ($\propto 10^6$) independent Monte-Carlo simulations of random walks and detected whether a trajectory of the particle ended up at the lower or at the upper boundary. The ratio between the number of cases when the particle stops on the upper boundary ($y_f = L_0$) and vice versa ($y_f = 0$), $I_{\text{up}}/I_{\text{d}}$, is calculated and plotted in Fig. 6 (examples of particle's trajectories are shown in the inset). In Figure 6 results for three previously considered types of scatterers are indicated by the solid markers: blue disk (quantum), red triangle (intermediate), and purple rhombus (classical). In addition, the cyan star gives the value of ratchet effect that was obtained within full Schrödinger equation simulations, see Fig. 5, in order to emphasize self-consistency of the approaches. In Figure 6, we also indicate by the green square marker the case of an uniform probability distribution which describes the scattering on a C_{6v} -symmetric defect and therefore absence of asymmetry in scattering.

One can note that the general structure and dominating elements of the asymmetric parts for all considered scattering matrices are similar, see Sec. II defects and *Supplementary*. As a result, it is possible to characterize of scattering matrix asymmetry by a single value as

$$s_f = \frac{\|A^{as}\|_F}{\|A^s\|_F + \|A^{as}\|_F}, \quad (5)$$

Here $A^{as(s)} = (A \mp A^T)/2$ is an anti-symmetric (symmetric) part of scattering matrix A and $\|\cdot\|$ denotes the Frobenius norm of a matrix (in principle, any matrix norm). The s_f values calculated for the scattering matrices of the treated defects, give the horizontal axis values

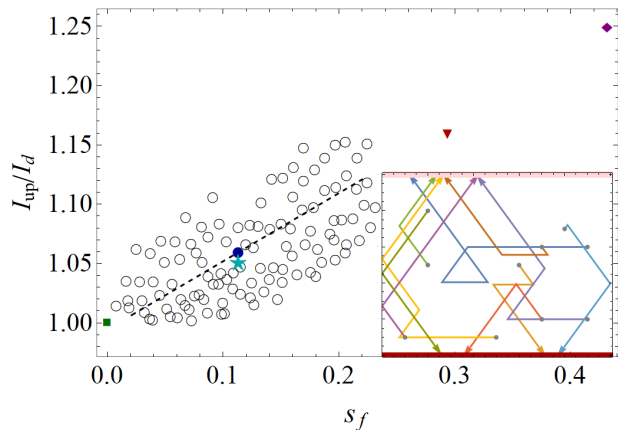


Figure 6. Illustration of the emergence of ratchet effect due to asymmetry in scattering in stochastic random-walk approach. The vertical axis shows ratio of upwards to downwards carrier fluxes. The horizontal axis is for a measure of scattering asymmetry. Blue star corresponds to the value obtained within the GPE simulations. Other colored markers represent results of Monte-Carlo simulations with scattering rates defined by the ones from full Schrödinger equation calculations. The empty circles are related to values of ratchet effect obtained with synthetic matrices (see the main text). The inset shows examples of the conspicuous particle's trajectories.

in Fig. 6.

Further, one can construct a synthetic scattering matrix of arbitrary degree of asymmetry based on the one corresponding to, e.g., to the quantum regime, see Fig. 4(b). Using the decomposition of a matrix into symmetric and anti-symmetric parts, one can utilize the following expression

$$\tilde{W}_{k,k'} = a_1 W_{k,k'}^{(as)} + a_2 (W_{k,k'}^{(s)} - W_{k,k}^{(s)}) + a_0 W_{k,k}^{(s)}, \quad (6)$$

with a definite value of asymmetry s_f adjusted by the coefficients $a_i, i = 1, 2, 0$. Here, a_1 controls the degree of asymmetry, a_2 gives the contribution from the off-diagonal symmetric part elements and a_0 is for the diagonal part. The normalization condition $\sum_{k'} \tilde{W}_{k,k'} = 1$ is also satisfied by tuning the amplitude of the coefficients. Noteworthy, various ratios between the coefficients can give the same measure of asymmetry s_f . Results of the Monte-Carlo simulations for multiple synthetic scattering matrices are presented by open circles in Fig. 6. One can note from Fig. 6 that ratchet current quantified by $I_{\text{up}}/I_{\text{d}}$ and emerged due to asymmetry in scattering processes, is linearly proportional to the asymmetry coefficient, s_f . This fact is in agreement with the predictions of Ref. [31] for the flux of noninteracting particles experienced elastic scattering in the medium which does not possess a center of symmetry. Additionally, one could note that the coefficient of asymmetry is, in turn, proportional to the characteristic size of a triangle: $s_f \propto L$.

V. CONCLUSIONS

We consider a way to reveal the presence of ratchet effect in the exciton-polariton analogue of graphene employing the phenomenon of skew (asymmetric) scattering on defects of triangular shape. Introducing such defects to regular honeycomb lattice violates the global spatial inversion symmetry (lowering the system symmetry to C_{3v}) and thus allows the appearance of ratchet flux. Within the framework of Schrödinger equation, we provide detailed numerical simulations of wave packet scattering by a single defect of triangular shape. The obtained scattering cross sections and indicatrices show the microscopic details of skew scattering both for optical graphene and its classical counterpart. Employing the similar calculations we show presence of macroscopic ratchet flux in the system of photonic graphene with

multiple coherently oriented triangular defects. Finally, we support the obtained results with stochastic random walks approach drawing the correspondence between observed in simulations global ratchet effect and scattering cross-sections. Present study provides microscopic insight into skew scattering phenomenon in graphene and makes the concept of ratchet phenomena to be widened on the field of photonics. The setup to experimentally measure the effect is proposed for the state-of-the-art etched microcavities with exciton-polaritons as well as other optical analogues of graphene.

ACKNOWLEDGEMENTS

We acknowledge the financial support from the Institute for Basic Science (IBS) in the Republic of Korea through the projects IBS-R024-Y3 and IBS-R024-D1 (O.M.B.).

-
- [1] C. Weisbuch, M. Nishioka, A. Ishikawa, and Y. Arakawa. Observation of the coupled exciton-photon mode splitting in a semiconductor quantum microcavity. *Physical Review Letters*, 69(23):3314–3317, December 1992.
 - [2] Alexey Kavokin and Guillaume Malpuech, editors. *Cavity polaritons*. Number v. 32 in Thin films and nanostructures. Elsevier, San Diego, 2003. Includes bibliographical references and index.
 - [3] Dmitry D. Solnyshkov, Guillaume Malpuech, Philippe St-Jean, Sylvain Ravets, Jacqueline Bloch, and Alberto Amo. Microcavity polaritons for topological photonics [invited]. *Optical Materials Express*, 11(4):1119, 2021.
 - [4] Thomas Boulier, Maxime J. Jacquet, Anne Maître, Giovanni Lerario, Ferdinand Claude, Simon Pigeon, Quentin Glorieux, Alberto Amo, Jacqueline Bloch, Alberto Bramati, and Elisabeth Giacobino. Microcavity polaritons for quantum simulation. *Advanced Quantum Technologies*, 3(11), August 2020.
 - [5] Jacqueline Bloch, Iacopo Carusotto, and Michiel Wouters. Non-equilibrium bose–einstein condensation in photonic systems. *Nature Reviews Physics*, 4(7):470–488, June 2022.
 - [6] J. Kasprzak, M. Richard, S. Kundermann, A. Baas, P. Jeambrun, J. M. J. Keeling, F. M. Marchetti, M. H. Szymańska, R. André, J. L. Staehli, V. Savona, P. B. Littlewood, B. Deveaud, and Le Si Dang. Bose–einstein condensation of exciton polaritons. *Nature*, 443(7110):409–414, September 2006.
 - [7] Alberto Amo, Jérôme Lefrère, Simon Pigeon, Claire Adrados, Cristiano Ciuti, Iacopo Carusotto, Romuald Houdré, Elisabeth Giacobino, and Alberto Bramati. Superfluidity of polaritons in semiconductor microcavities. *Nature Physics*, 5(11):805–810, September 2009.
 - [8] Iacopo Carusotto and Cristiano Ciuti. Quantum fluids of light. *Reviews of Modern Physics*, 85(1):299–366, February 2013.
 - [9] Tim Byrnes, Na Young Kim, and Yoshihisa Yamamoto. Exciton–polariton condensates. *Nature Physics*, 10(11):803–813, October 2014.
 - [10] D. D. Solnyshkov, H. Terças, K. Dini, and G. Malpuech. Hybrid boltzmann–gross-pitaevskii theory of bose–einstein condensation and superfluidity in open driven-dissipative systems. *Physical Review A*, 89(3):033626, March 2014.
 - [11] K. G. Lagoudakis, M. Wouters, M. Richard, A. Baas, I. Carusotto, R. André, Le Si Dang, and B. Deveaud-Plédran. Quantized vortices in an exciton–polariton condensate. *Nature Physics*, 4(9):706–710, August 2008.
 - [12] T Boulier, H Terças, DD Solnyshkov, Q Glorieux, E Giacobino, G Malpuech, and A Bramati. Vortex chain in a resonantly pumped polariton superfluid. *Scientific reports*, 5(1):9230, 2015.
 - [13] Natalia G. Berloff. Turbulence in exciton-polariton condensates. 2010.
 - [14] M. T. Reeves, B. P. Anderson, and A. S. Bradley. Classical and quantum regimes of two-dimensional turbulence in trapped bose-einstein condensates. *Physical Review A*, 86(5):053621, November 2012.
 - [15] S.V. Koniakhin, O. Bleu, G. Malpuech, and D.D. Solnyshkov. 2d quantum turbulence in a polariton quantum fluid. *Chaos, Solitons & Fractals*, 132:109574, 2020.
 - [16] E. Wertz, L. Ferrier, D. D. Solnyshkov, R. Johne, D. Sanvitto, A. Lemaître, I. Sagnes, R. Grousson, A. V. Kavokin, P. Senellart, G. Malpuech, and J. Bloch. Spontaneous formation and optical manipulation of extended polariton condensates. *Nature Physics*, 6(11):860–864, August 2010.
 - [17] Lydie Ferrier, Esther Wertz, Robert Johne, Dmitry D. Solnyshkov, Pascale Senellart, Isabelle Sagnes, Aristide Lemaître, Guillaume Malpuech, and Jacqueline Bloch. Interactions in confined polariton condensates. *Physical Review Letters*, 106(12):126401, 2011.
 - [18] Marta Galbiati, Lydie Ferrier, Dmitry D Solnyshkov, Dimitrii Tanese, Esther Wertz, Alberto Amo, Marco Abbarchi, Pascale Senellart, Isabelle Sagnes, Aristide Lemaître, et al. Polariton condensation in photonic molecules. *Physical review letters*, 108(12):126403, 2012.

- [19] D.D. Solnyshkov, A.V. Nalitov, and G. Malpuech. Kibble-zurek mechanism in topologically nontrivial zigzag chains of polariton micropillars. *Physical Review Letters*, 116(4):046402, 2016.
- [20] Tristan H Harder, Meng Sun, Oleg A Egorov, Ihor Vakulchyk, Johannes Beierlein, Philipp Gagel, Monika Emmerling, Christian Schneider, Ulf Peschel, Ivan G Savenko, et al. Coherent topological polariton laser. *ACS Photonics*, 8(5):1377–1384, 2021.
- [21] Philip Richard Wallace. The band theory of graphite. *Physical review*, 71(9):622, 1947.
- [22] A.V. Nalitov, G. Malpuech, H. Terças, and D.D. Solnyshkov. Spin-orbit coupling and the optical spin hall effect in photonic graphene. *Physical Review Letters*, 114(2):026803, 2015.
- [23] Mourad Oudich, Guangxu Su, Yuanchen Deng, Wladimir Benalcazar, Renwen Huang, Nikhil J. R. K. Gerard, Minghui Lu, Peng Zhan, and Yun Jing. Photonic analog of bilayer graphene. *Phys. Rev. B*, 103:214311, Jun 2021.
- [24] Zhaoyang Zhang, Yuan Feng, Feng Li, Sergei Koniakhin, Changbiao Li, Fu Liu, Yanpeng Zhang, Min Xiao, Guillaume Malpuech, and Dmitry Solnyshkov. Angular-dependent klein tunneling in photonic graphene. *Physical Review Letters*, 129(23):233901, 2022.
- [25] D. D. Solnyshkov, O. Bleu, and G. Malpuech. Topological optical isolator based on polariton graphene. *Applied Physics Letters*, 112(3), 2018.
- [26] O. M. Bahrova, S. V. Koniakhin, A. V. Nalitov, and E. D. Cherotchenko. Optical snake states in a photonic graphene. *Opt. Lett.*, 49(10):2581–2584, May 2024.
- [27] Søren Schou Gregersen, Stephen R. Power, and Antti-Pekka Jauho. Nanostructured graphene for spintronics. *Physical Review B*, 95(12):121406, March 2017.
- [28] Alexey Kavokin, Timothy C. H. Liew, Christian Schneider, Pavlos G. Lagoudakis, Sebastian Klemmt, and Sven Hoefling. Polariton condensates for classical and quantum computing. *Nature Reviews Physics*, 4(7):435–451, April 2022.
- [29] Luciano S. Ricco, Ivan A. Shelykh, and Alexey Kavokin. Qubit gate operations in elliptically trapped polariton condensates. *Scientific Reports*, 14(1), February 2024.
- [30] Dmitry Solnyshkov, Anton Nalitov, Berihu Teklu, Louis Franck, and Guillaume Malpuech. Spin-dependent klein tunneling in polariton graphene with photonic spin-orbit interaction. *Physical Review B*, 93(8):085404, 2016.
- [31] V I Belinicher and B I Sturman. The photogalvanic effect in media lacking a center of symmetry. *Soviet Physics Uspekhi*, 23(3):199–223, 1980.
- [32] C. Drexler, S. A. Tarasenko, P. Olbrich, J. Karch, M. Hirmer, F. Müller, M. Gmitra, J. Fabian, R. Yakimova, S. Lara-Avila, S. Kubatkin, M. Wang, R. Vajtai, P. M. Ajayan, J. Kono, and S. D. Ganichev. Magnetic quantum ratchet effect in graphene. *Nature Nanotechnology*, 8(2):104–107, 2013.
- [33] Søren Schou Gregersen, Jose H Garcia, Antti-Pekka Jauho, Stephan Roche, and Stephen R Power. Charge and spin transport anisotropy in nanopatterned graphene. *Journal of Physics: Materials*, 1(1):015005, September 2018.
- [34] Sergei V. Koniakhin. Ratchet effect in graphene with trigonal clusters. *The European Physical Journal B*, 87(9), 2014.
- [35] A. V. Nalitov, L. E. Golub, and E. L. Ivchenko. Ratchet effects in two-dimensional systems with a lateral periodic potential. *Physical Review B*, 86(11):115301, 2012.
- [36] E. Mönch, S. O. Potashin, K. Lindner, I. Yahniuk, L. E. Golub, V. Yu. Kachorovskii, V. V. Bel’kov, R. Huber, K. Watanabe, T. Taniguchi, J. Eroms, D. Weiss, and S. D. Ganichev. Ratchet effect in spatially modulated bilayer graphene: Signature of hydrodynamic transport. *Physical Review B*, 105(4):045404, 2022.
- [37] P. Olbrich, J. Kamann, M. König, J. Munzert, L. Tutsch, J. Eroms, D. Weiss, Ming-Hao Liu, L. E. Golub, E. L. Ivchenko, V. V. Popov, D. V. Fateev, K. V. Mashinsky, F. Fromm, Th. Seyller, and S. D. Ganichev. Terahertz ratchet effects in graphene with a lateral superlattice. *Physical Review B*, 93(7):075422, February 2016.
- [38] G. V. Budkin, L. E. Golub, E. L. Ivchenko, and S. D. Ganichev. Magnetic ratchet effects in a two-dimensional electron gas. *JETP Letters*, 104(9):649–656, November 2016.
- [39] S. Bellucci, L. Pierantoni, and D. Mencarelli. Ballistic ratchet effect on patterned graphene. *Integrated Ferroelectrics*, 176(1):28–36, November 2016.
- [40] Davide Mencarelli, Gian Marco Zampa, and Luca Pierantoni. Current-voltage characterization of multi-port graphene based geometric diodes for high-frequency electromagnetic harvesting. *IEEE Access*, 10:123251–123258, 2022.
- [41] AD Chepelianskii, MV Entin, LI Magarill, and DL Shepelyansky. Photogalvanic current in artificial asymmetric nanostructures. *The European Physical Journal B*, 56:323–333, 2007.
- [42] Leonardo Ermann and Dima L Shepelyansky. Relativistic graphene ratchet on semidisk galton board. *The European Physical Journal B*, 79:357–362, 2011.
- [43] M. Hild, L. E. Golub, A. Fuhrmann, M. Otteneder, M. Kronseder, M. Matsubara, T. Kobayashi, D. Oshima, A. Honda, T. Kato, J. Wunderlich, C. Back, and S. D. Ganichev. Terahertz spin ratchet effect in magnetic metamaterials. *Physical Review B*, 107(15):155419, April 2023.
- [44] B. Real, O. Jamadi, M. Milićević, N. Pernet, P. St-Jean, T. Ozawa, G. Montambaux, I. Sagnes, A. Lemaître, L. Le Gratiet, A. Harouri, S. Ravets, J. Bloch, and A. Amo. Semi-dirac transport and anisotropic localization in polariton honeycomb lattices. *Physical Review Letters*, 125(18):186601, 2020.
- [45] Omar Jamadi, Elena Rozas, Grazia Salerno, Marijana Milićević, Tomoki Ozawa, Isabelle Sagnes, Aristide Lemaître, Luc Le Gratiet, Abdelmounaim Harouri, Iacopo Carusotto, Jacqueline Bloch, and Alberto Amo. Direct observation of photonic landau levels and helical edge states in strained honeycomb lattices. *Light: Science & Applications*, 9(1), 2020.
- [46] Zhaoyang Zhang, Feng Li, Yiqi Zhang, Changbiao Li, Yanpeng Zhang, Min Xiao, and DD Solnyshkov. Particlelike behavior of topological defects in linear wave packets in photonic graphene. *Physical Review Letters*, 122(23):233905, 2019.
- [47] Feng Li, Sergei V Koniakhin, Anton V Nalitov, Evgeniia Cherotchenko, Dmitry D Solnyshkov, Guillaume Malpuech, Min Xiao, Yanpeng Zhang, and Zhaoyang Zhang. Simultaneous creation of multiple vortex-antivortex pairs in momentum space in photonic lattices. *Advanced Photonics*, 5(6):066007–066007, 2023.
- [48] Craig F. Bohren and Donald R. Huffman. *Absorption and scattering of light by small particles*. Wiley-VCH,

Weinheim, 2004. Literaturverzeichnis: Seite 499-519 und Index.

Supplemental Material: Skew scattering and ratchet effect in exciton-polariton analogues of graphene

O.M. Bahrova^{1,2}, and S.V. Koniakhin^{1,3}

¹ *Center for Theoretical Physics of Complex Systems,
Institute for Basic Science (IBS), Daejeon 34126, Republic of Korea*

² *B. Verkin Institute for Low Temperature Physics and Engineering of the National
Academy of Sciences of Ukraine, 47 Nauky Ave., Kharkiv 61103, Ukraine*

³ *Basic Science Program, Korea University of Science and Technology (UST), Daejeon 34113, Republic of Korea*

LIST OF FIGURES

Figure S1. Scattering diagram $W_{0^\circ, k'}$ and scattering rate matrix for intermediate regime;

Figure S2. Additional scattering diagrams (compare with Figs. 3-4 of the main text);

Figure S3. Dependencies of asymmetry vector components on the triangle size and the wave vector value for scattering diagrams Fig. S2;

Figure S4. An example of the wave function initial conditions used in 2D simulations of Schrödinger equation discussed in Sec III of the main text;

Figure S5. Results of Schrödinger equation calculations analyzed in Sec III of the main text, demonstrating the emergence of ratchet effect.

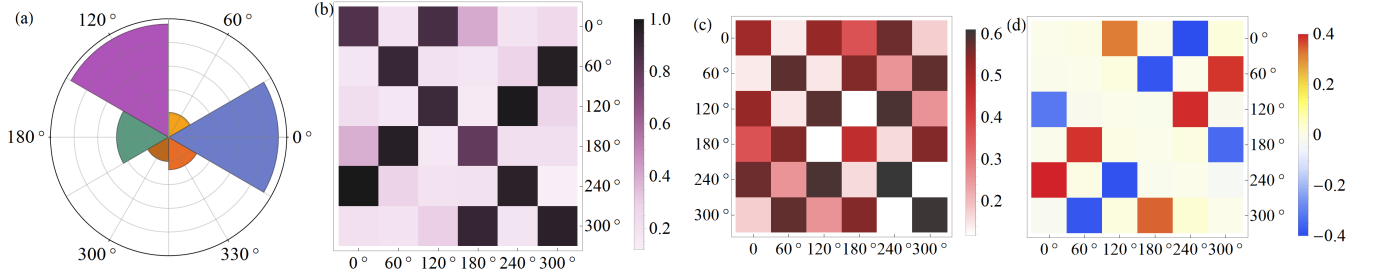


Figure S1. Real space scattering rate $W_{k,k'}$ in the "intermediate" regime normalized on the maximum (b). (a) scattering diagram $W_{0^\circ, k'}$ representing in essence the first row of the matrix shown in (b). The symmetric (c) $W_{k,k'}^{(s)}$ and anti-symmetric (d) $W_{k,k'}^{(as)}$ parts of the scattering matrix $W_{k,k'}$ (b).

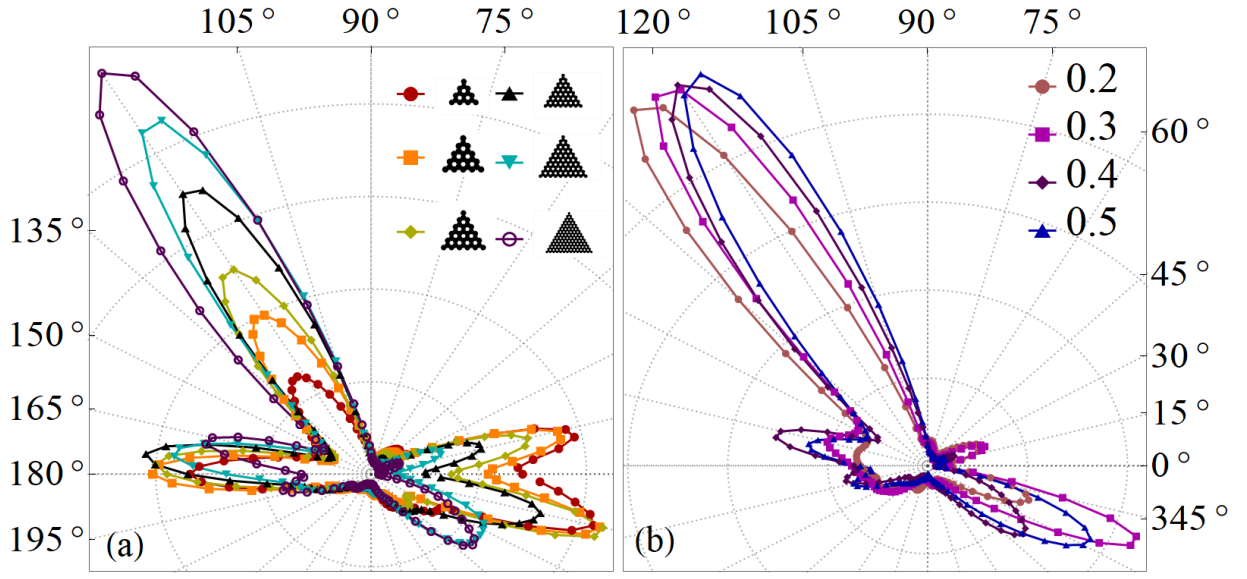


Figure S2. (a) Scattering diagrams for various sizes of triangle defect and $q = 0.4$ (compare with the subfigure (a) in Fig. 2 of the main text). (b) Scattering diagrams for different values of initial wave vector for the regime of classical scattering. The purple curve is the same as one in (a).

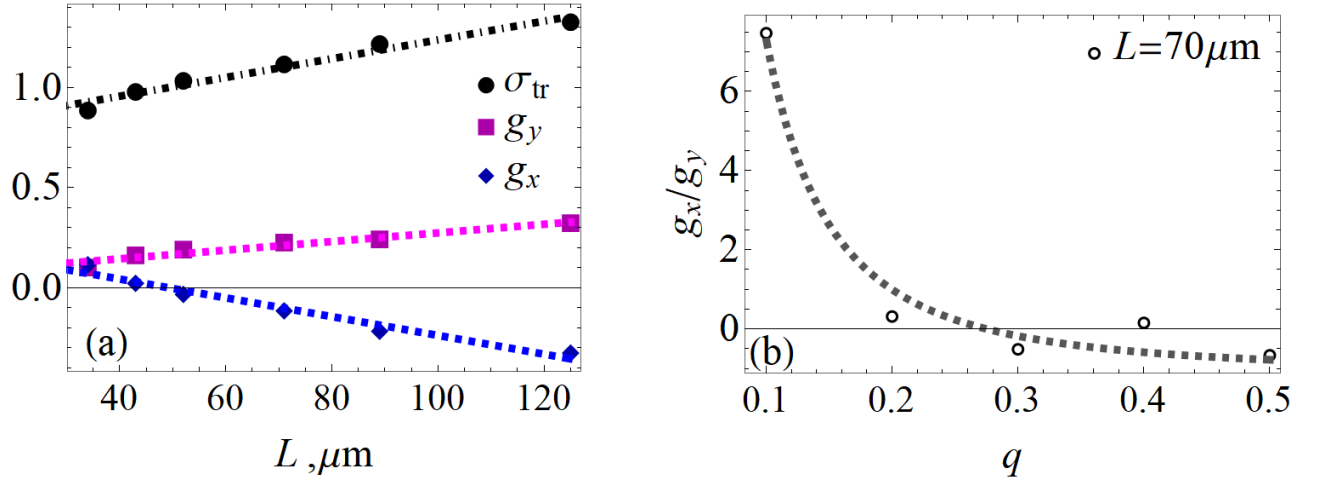


Figure S3. (a) Asymmetry parameter along the horizontal (g_x) and vertical (g_y) axes calculated for the scattering diagrams presented in Fig. S2(a). Additionally, black dots indicate the transport cross-section values σ_{tr} . See also plot (c) in Fig. 2 of the main text. (b) The ratio of g_x/g_y versus initial wave vector values q measured from the Dirac point one.

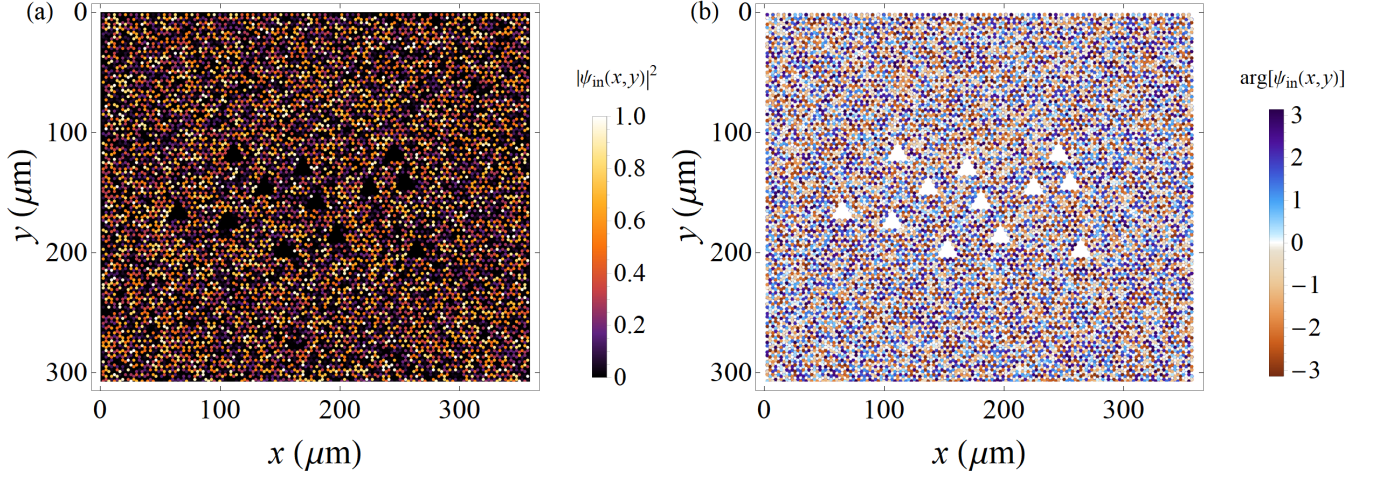


Figure S4. An example of random initial conditions used in numerical simulations of GPE in order to obtain the ratchet effect (see Fig. 5 of the main text). The initial wave function is chosen to be uniform random distribution for the amplitude (a) and phase (b) (a number is assigned for each lattice site (micropillar)). There is evidently no initially introduced preferential direction of motion. A sequence of prepared in a such way initial wave function with also randomly distributed triangle defects located in the central part of the sample, was used.

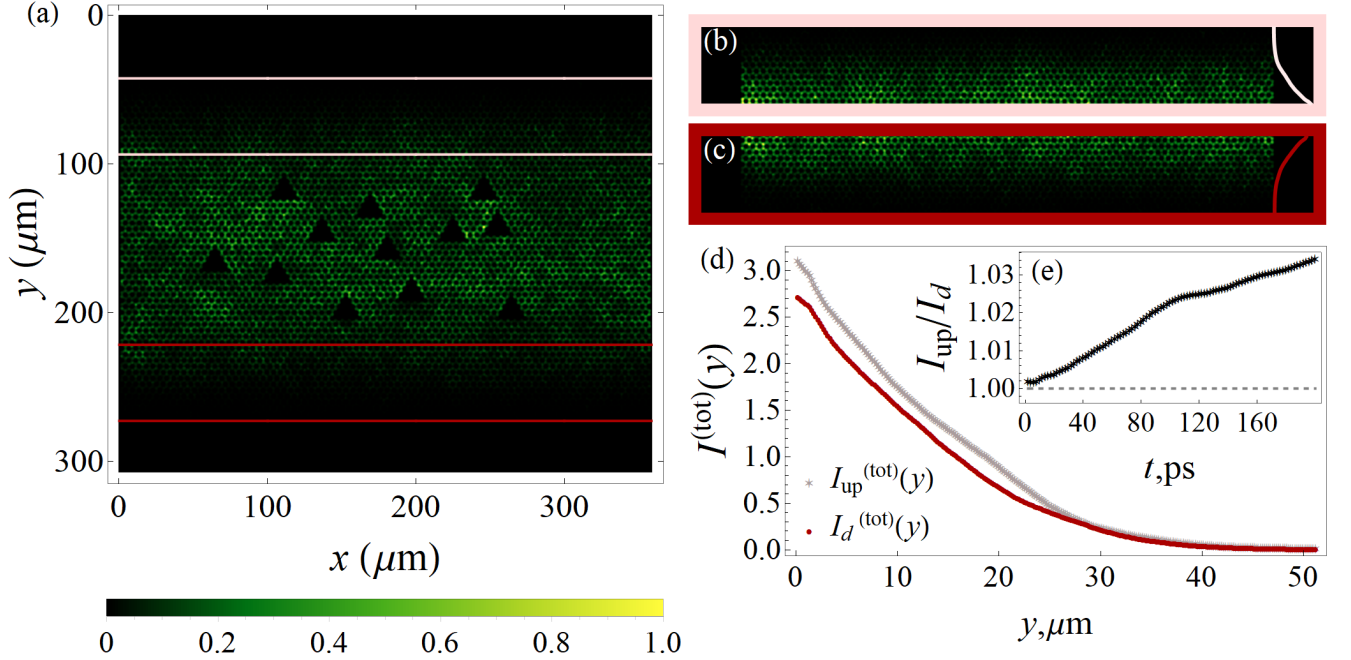


Figure S5. Time-averaged intensity (up to $t = 190\text{ps}$). (e) The ratio of time-averaged wave function in upper region I_{up} to the one in lower counting region I_{d} versus time (averaged over >40 cases including shifts of the symmetry line of counting regions in respect to the defects center of mass and two different decay rates). In order to emphasize the difference in intensities, we plot $|\psi(x,y)|^6$ in (a).